# Comparison of a Standard Resolution PET-CT Scanner With an HRRT Brain Scanner for Imaging Small Tumors Within the Head

Jose M. Anton-Rodriguez, Peter Julyan, Ibrahim Djoukhadar, David Russell, D. Gareth Evans, Alan Jackson, and Julian C. Matthews

***Abstract*—We compared a conventional PET-CT scanner (Siemens Biograph TruePoint TrueV) with and without resolution modeling (RM) image reconstruction with a high resolution research tomograph (HRRT) in order to assess the utility of conventional scanners for brain scanning. A modified Esser phantom and 6 neurofibromatosis 2 (NF2) patients with vestibular schwannomas (VS) were scanned using both scanners. The phantom was filled with fluorine-18 (40 MBq, 4:1 contrast ratio) and scanned for 60 min on separate occasions. Patients were injected with ∼200 MBq of [$^{18}$F]fluorodeoxyglucose (FDG) and [$^{18}$F]fluorothymidine (FLT) on separate occasions and scanned for three consecutive 30 min periods moving between scanners. The HRRT images, although noisier, resulted in higher contrast recovery for the smallest cylindrical inserts in comparison to TrueV with and without RM. With the TrueV, higher uptake values were observed in VS lesions with both FDG and FLT which is consistent with greater spill-in from the brain for FDG and bone marrow for FLT. RM decreased measured FDG uptake. For large homogenous lesions the conventional TrueV gives similar or better results compared to the HRRT. For smaller lesions, the HRRT has benefit, with RM on the TrueV unable to restore parity, and with the potential for image artifacts.**

***Index Terms*—High resolution PET, high resolution research tomograph (HRRT), resolution modeling (RM).**

Manuscript received October 1, 2018; revised February 8, 2019 and April 16, 2019; accepted April 23, 2019. Date of publication May 3, 2019; date of current version July 1, 2019. This work was supported by the Cancer Research U.K. and Engineering and Physical Sciences Research Council Cancer Imaging Centre in Cambridge and Manchester under Grant C8742/A18097. The work of J. M. Anton-Rodriguez was supported in part by The Christie NHS Foundation Trust and in part by the University of Manchester. *(Corresponding author: Jose M. Anton-Rodriguez.)*

J. M. Anton-Rodriguez is with the Division of Informatics, Imaging and Data Sciences, MAHSC, University of Manchester, Manchester M20 3LJ, U.K., and also with the Christie Medical Physics and Engineering, The Christie NHS Foundation Trust, Manchester M20 4BX, U.K. (e-mail: jose.anton@manchester.ac.uk).

P. Julyan is with the Christie Medical Physics and Engineering, The Christie NHS Foundation Trust, Manchester M20 4BX, U.K.

I. Djoukhadar and D. Russell are with the Division of Informatics, Imaging and Data Sciences, MAHSC, University of Manchester, Manchester M20 3LJ, U.K.

D. G. Evans is with Genomic Medicine, Central Manchester University Hospital, NHS Foundation Trust, Manchester M13 9WL, U.K.

A. Jackson and J. C. Matthews are with the Division of Neuroscience and Experimental Psychology, MAHSC, University of Manchester, Manchester M20 3LJ, U.K.

Color versions of one or more of the figures in this paper are available online at http://ieeexplore.ieee.org.

Digital Object Identifier 10.1109/TRPMS.2019.2914909

## I. Introduction

THE high resolution research tomograph (HRRT, Siemens Molecular Imaging) is a dedicated brain scanner designed for high spatial resolution imaging and is capable of achieving spatial resolutions of 2–3-mm full width at half maximum (FWHM) [1]. This is achieved using small detector crystals of 2.1 mm × 2.1 mm and a multiscintillator (double crystal layer of LSO/LYSO of 10-mm thickness each layer) phoswich detector design that provides depth of interaction (DOI) discrimination and which results in improved image resolution off axial center [2], [3].

Commercially available PET scanners are generally multimodality, either PET-CT or more recently PET-MR, and are principally designed and optimized for whole body (WB) imaging (with improved sensitivity and improved electronics that enable higher count rate performance and TOF capability). Over the last 20 years the resolution of clinical PET scanners has not improved significantly with scanners of resolutions of around 4–5-mm FWHM as with the Siemens Biograph 6 TruePoint TrueV (Siemens Molecular Imaging) used in this paper. WB scanners have larger ring detector diameters, bigger crystals sizes and do not have DOI capability. However, recently a new commercial WB system [Biograph Vision (Siemens)] with improved spatial resolution of around 3.2-mm FWHM has been made available which might mark a new trend in WB scanners [4]. A new generation of dedicated high resolution brain scanners are starting to be commercially available using silicon photomultipliers (SiPMs) technology resulting in portable or transferable scanners with comparable resolution to the HRRT but improved sensitivity such the NeuroPET system (Photo Diagnostic System) [5], the CareMiBrain (Oncovision) [6], the MINDView PET insert [7], the TRIMAGE project [8], and some other efforts being reported at a more experimental level with a wearable PET scanner that can move with head movements [9]. However, to our knowledge, these scanners are yet to establish themselves and the benefit of high resolution in clinical PET remains unclear. In addition, a recent review on organ-dedicated (e.g., brain, cardiac, breast etc.) PET systems and single photon emission tomography (SPECT) systems can be found in [10].

In order to further improve spatial resolution, resolution modeling (RM) reconstruction algorithms which incorporate resolution blurring models may be considered as a software alternative to hardware approaches as reviewed in [11].

RM reconstructions attempts with a series of simplifications, to account for the effect that positron range, photon noncollinearity, and detection deficiencies, such as parallax errors and intercrystal scatter, have on resolution. For the Siemens Biograph (referred commercially to HD-PET) this is implemented in projection space and this implementation attempts to fully recover axially and radially the deterioration on resolution [12]. For the HRRT the RM is modeled in image space using a point spread function (PSF) [13], [14]. This implementation is regarded as a conservative approach, since the PSF used is spatially invariant and is narrower than that obtained from measured data, which will result in only a partial recovery of resolution. The incorporation of RM within PET reconstruction, in addition to improving image resolution [15], has been reported to decrease voxel variance [14], count dependent bias [16], and improved quantification by reducing partial volume effects in clinical brain studies [17]. However, the use of RM reconstruction comes with the penalty of slower rates of convergence, possible higher region of interest (ROI) variance [18], and generation of Gibbs artefacts [19].

In this paper, we perform a comparison between the HRRT [1], the highest spatial resolution human brain PET scanner, and a standard resolution WB PET-CT scanner, a Siemens Biograph Truepoint TrueV [20], for imaging small tumors in the head. A combination of patient and phantom data has been used to assess quantitative and qualitative differences of images with list mode (LM) bootstrapping techniques used to assess precision. We also explored whether RM image reconstruction can play a role in achieving image quality close to that of a dedicated brain scanner such the HRRT. Our motivation is to assess how good a standard resolution multimodality PET-CT scanner is for brain scanning, an application where high resolution is expected to be of benefit.

## II. Materials and Methods

### A. Modified Esser Phantom

The phantom is made of acrylic and consists of a cylindrical body with inner diameter of 204 mm and several thin walled cylindrical inserts of varying diameters. The phantom was modified by replacing two of the three 25-mm diameter cylinders with smaller cylinders of the same length (40 mm) resulting in cylinder diameters of 4, 6, 8, 12, 16, and 25 mm. Two set of acquisitions for each scanner were acquired. For the first set, all cylinders and main body were filled with fluorine-18 with a contrast ratio of approximately 4:1 in the cylinders to main body ("set 1") and for the second set the acquisition was repeated but with the 25-mm cylinder containing "cold" water ("set 2"). For all acquisitions, the total activity in the phantom was approximately 40 MBq at the start of scan with data acquired for duration of 60 min. For attenuation correction, 6 min transmission scans were acquired for the HRRT [21] and CT scans acquired for the TrueV. In addition aliquots of approximately 1 ml were taken and measured in a calibrated well counter to calculated true contrast ratios.

### B. Neurofibromatosis 2 Patients

Six patients with neurofibromatosis 2 (NF2) [22] were recruited as part of a clinical study at our centre [23]. As typical for NF2 condition, patients had multiple intracranial tumors (meningiomas and schwannomas) including at least one vestibular schwannoma (VS). Morphology and location of VS lesions together with the choice of tracer meant that challenges with the limited resolution of PET were envisaged. The study was approved by an independent research ethics committee and by the United Kingdom Administration of Radioactive Substances Advisory Committee (ARSAC RPC 595/3586/30119). All patients gave informed written consent.

Patients were placed on one of the two scanners and injected with a target dose of 200 MBq of fluorodeoxyglucose (FDG) (with a fast period of 6 h prior injection) or fluorothymidine (FLT), with data acquired for 60 min following injection (scan 1). Following a short break the patients were placed on the other scanner, with data acquired for 30 min (scan 2). Finally, following a second short break the patient was placed on the original scanner with data acquired for 30 min (scan 3). On a different scanning day the procedure was repeated in the same patient using the alternative radiotracer. Scans 1 and 3 were conducted using the HRRT scanner in three patients and the TrueV in the other three patients. Breaks between scans varied between 10 and 20 min. For attenuation correction, transmission scans were acquired on the HRRT (preinjection for scan 1 and post emission for scans 2 and 3) with pre-emission CT scans on the TrueV. MRI scans that were acquired as part of the patient's normal care were used for anatomical information using a contrast enhanced high-resolution $T_1$-weighted whole brain volume acquisition.

### C. Image Reconstruction

Patient data and phantom data were acquired in list-mode for both scanners. Data during the last 30 min of scan 1 and for scans 2 and 3 for the patient data and the full 60-min phantom scan data were used for the reconstructions. The axial compression or span that is typical for these two scanners was used and was 9 for the HRRT and 11 for the TrueV. In addition, LM bootstrapping resampling was used on the set 2 data of the Esser phantoms and on the patient data for both scanners to create 50 resampled realizations [24]–[26].

For both scanners implementations of 3-D iterative ordinary Poisson ordered subset expectation maximization (OP-OSEM) [27] without (No-RM) and with RM were used. For the HRRT the users' community software was used with an OP-OSEM implementation described in [28].

The RM for the HRRT is modeled as spatially invariant double isotropic Gaussian function with $\sigma_1 = 0.9$ mm, $\sigma_2 = 2.5$ mm, and mixing term $\rho = 0.05$ (corresponding to the default reconstruction kernel) using the nomenclature of Comtat *et al.* [13]. Up to 25 iterations using 16 subsets were conducted with images returned consisting of $256 \times 256 \times 207$ voxels each of size 1.22 mm $\times$ 1.22 mm $\times$ 1.22 mm. For the TrueV the offline reconstruction Siemens package e7_tools was used. The RM on the TrueV is modeled as nonstationary

in projection space with the product of parametrized functions in the radial and axial directions and for these reconstructions the default RM settings were used. Up to 25 iterations were performed with 21 subsets using an image zoom of 2 resulting in images with voxel sizes of 1.33 mm × 1.33 mm × 2.03 mm and an image grid dimension of $256 \times 256 \times 109$ voxels. All reconstructions for both scanners were performed with corrections for scatter and attenuation. For the HRRT and for patient data an image of the attenuation coefficient was derived using the total variation (TXTV) method [29]. On patient data, the attenuation maps of each scanning session were co-registered to the first 10 min of emission data to reduce artifacts due to EM-TX mismatches during reconstruction for both scanners [30].

### D. Esser Phantom Data Analysis

Analysis of the phantom was based on the image quality section of the NEMA standards [31], with modification to accommodate differences between the NEMA image quality and Esser phantoms. Specifically, circular ROIs with diameters equal to that of each cylindrical insert were drawn on five adjacent planes and within each of the six hot inserts (4, 6, 8, 12, 16, and 25-mm diameters). In addition for each of the six cylinder sizes and each of the five planes, 12 background regions were drawn in different locations but on the same transverse planes and using the same transaxial ROI size as for the hot regions ($K = 60$ cylinders of $D = 6$ different diameters). The contrast recovery coefficient ($\mathrm{CRC}_d$) for the $d$th hot and cold cylinders were calculated using

$$\mathrm{CRC}_d^{\mathrm{hot}} = \frac{\frac{\bar{C}_d}{\bar{B}_d} - 1}{\mathrm{CR}_{\mathrm{WC}} - 1} \cdot 100 \tag{1}$$

$$\mathrm{CRC}_d^{\mathrm{cold}} = \frac{\bar{B}_d - \bar{C}_d}{\bar{B}_d} \cdot 100 \tag{2}$$

where $\bar{C}_d$ and $\bar{B}_d$ are the mean radioactivity concentration within the $d$th cylinder and background regions averaged over the multiple ROIs and $\mathrm{CR}_{\mathrm{WC}}$ is the contrast ratio determined from the aliquots. In addition, the coefficient of variation (COV) of the contrast recovery coefficient (CRC) values was calculated using the bootstrap realization as a measure of their precision.

Image roughness (IR) [32], which measures the pixel to pixel variability in the image and is defined as the COV of the pixel values, was calculated for each background region size and averaged across the background ROIs as (following notation of Tong *et al.*):

$$\mathrm{IR}_{d,r,k} = \frac{\sqrt{\frac{1}{I_d - 1} \cdot \sum_{i=1}^{I_d} \left(f_{d,i,r} - \bar{B}_{d,r,k}\right)^2}}{\bar{B}_{d,r,k}} \cdot 100 \tag{3}$$

where $f_{d,i,r}$ is the reconstructed value at pixel $i$ for realization $r$ in cylinder size $d$, and $\bar{B}_{d,r,k}$ is the mean value of voxel concentrations within the $k$th background ROI and which has $I_d$ voxels. This value was averaged over all background ROIs to generate, $\mathrm{IR}_{d,r}$, which can be further averaged over the bootstrap realizations to obtain $\mathrm{IR}_d$.

Ensemble noise (EN) was also calculated over the multiple realizations in the background regions which is considered to be inversely proportional to detection task performance [32]. For each ROI it is defined as the COV of ROI means across the $R = 50$ realizations

$$\mathrm{EN}_{d,k} = \frac{1}{R} \cdot \sum_{r=1}^{R} \frac{\sigma_{d,r,k}}{\bar{M}_{d,r,k}} \cdot 100 \tag{4}$$

where $\sigma_{d,r,k}$ and $\bar{M}_{d,r,k}$ are the standard deviation and mean values, respectively of voxel concentrations within the $k$th background ROI for the $d$th cylinder ROI size over the $r$th realization. $\mathrm{EN}_{d,k}$ can be further averaged over the 60 ROIs to obtain a $\mathrm{EN}_d$ for each ROI size.

### E. NF2 Patient Data Analysis

MRI-contrast enhanced $T_1$-weighted images from each patient were co-registered to PET images for each of the three scans using rigid body transformations and statistical parametric mapping (SPM) version 8 (FIL, UCL, London). Volumes of interest (VOI) were manually drawn on the contrast enhanced portion of lesions. The VOI regions were applied to each registered PET images to extract mean decay corrected standardized uptake values (SUVs). Using linear interpolation, values during scan 2 were estimated from the measurements during scans 1 and 3. This was then used to examine quantitative differences in the measurements between the two scanners. For the patient data, reconstructions with 10 iterations without RM and 12 iterations with RM were used.

## III. Results

### A. Qualitative Comparison of the Esser Phantom

Coronal and transverse slices of the mean and standard deviation (std dev) images on the Esser phantom of the set 2 data over the bootstrap replicates for both scanners, both without (10 iterations) and with RM (12 iterations), are shown in Fig. 1. The range and scale are the same for both scanners (std dev range 0–4 KBq/ml and for the mean 0–15 KBq/ml). For the mean images the TrueV images have less voxel noise than the HRRT images, both with and without RM. When using RM, for both scanners, voxel noise is lower but apparently more spatially correlated. For the smallest cylinder, higher contrast is observed on the HRRT images and when RM is used (as expected with higher resolution). For the TrueV images with RM, significant edge overshooting or Gibbs artifacts are observed which are not seen with the HRRT (purple arrows in figure). For the images of voxel standard deviation the following observations can be made: 1) the voxel variance is approximately proportional to mean value with an additional axial effect (the phantom was positioned on both scanners with the hot cylinders positioned close to the axial center with the observed high variance toward to the edge of the axial field of view); 2) lower voxel variance results when using RM compared to No-RM for both scanners; and 3) higher voxel variance is seen for the HRRT compared to the TrueV for both No-RM and RM. In addition, (results not shown) the voxel variance increased with the number of iterations (HRRT/TrueV and No-RM/RM).

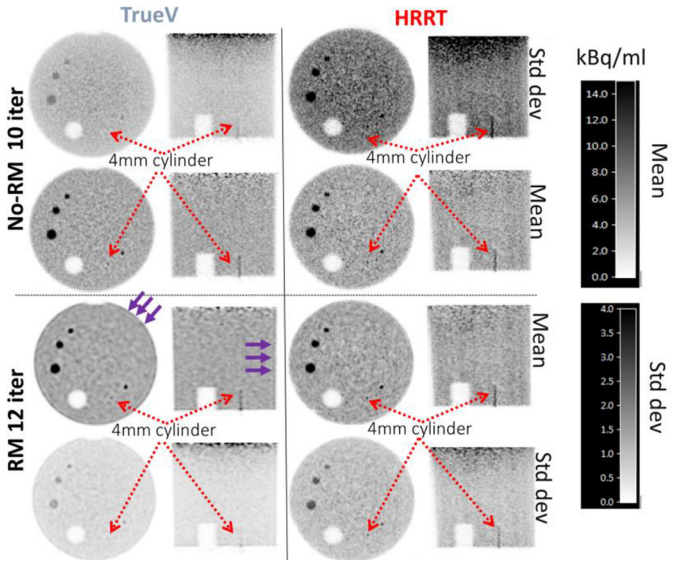


Fig. 1. Horizontal and transaxial images of the mean and standard deviation images on the Esser phantom set 2 data over the bootstrap replicates for the TrueV (No-RM/RM) and HRRT (No-RM/RM) reconstructed without (top images—10 iterations) and with RM (lower—12 iterations). Artifacts can be seen on the phantom edge with RM for the TrueV but not for the HRRT (purple arrows). The cylindrical inserts are centered axially within the scanner field of views.

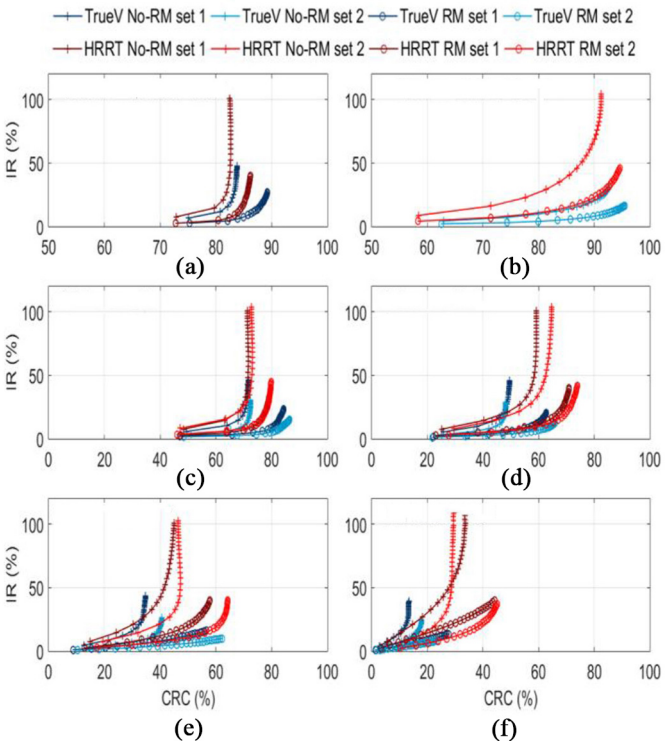


Fig. 2. IR versus CRC curves for cylinders of: a) 25-mm hot; b) 25-mm cold; c) 12 mm; d) 8 mm; e) 6 mm; and f) 4-mm diameter. Images reconstructed from iterations 1 to 25 (21 subsets for the TrueV and 16 subsets for the HRRT).

### *B. Quantitative Comparison of the Esser Phantom*

*1) Contrast Recovery and Voxel Noise:* CRC versus IR plots showing curves as iterations increase (up to 25 iterations) for both scanners are shown in Fig. 2 for: the cylindrical inserts of diameter 4, 6, 8, and 12 mm (sets 1 and 2); for the hot 25 mm insert (set 1 only) and cold 25 mm insert (set 2 only). For the cold 25-mm cylinder lower CRC is seen on the HRRT compared to the TrueV (around 5%) unless RM is used on the HRRT. In general good agreement is seen between the two data sets (sets 1 and 2) for both scanners with larger differences observed with the smaller inserts. The results for the 16-mm cylinder (not shown) follow similar trends to that of the 12 and hot 25-mm diameter cylinder. All the graphs in Fig. 2 show improvements in CRC and IR when RM is used. For hot cylinders with diameter greater or equal to 12 mm, the highest CRC values are observed for the TrueV images with RM which is likely to reflect the use of a less conservative RM approach. The TrueV images also have lower IR both with and without RM.

As the cylinder size is reduced from 8 to 4 mm, the CRC values with the HRRT become greater than the TrueV. Specifically comparing the TrueV RM to the HRRT No-RM reconstructions when a high number of iterations are used we observe the following: higher values are seen with the TrueV for the 8-mm cylinder; similar values for the 6-mm cylinder; and lower values for the 4-mm cylinder. CRC values are still converging after 25 iterations for cylinders $<8$ mm diameter, with greater dependency on iteration number when RM is used which is more marked as the cylinder diameter decreases. For the 4-mm cylinder CRC values have not converged by 25 iterations for either scanner.

*2) Bootstrap Resampled Data:* EN measured over the background regions using 50 bootstrap realizations on the set 2, $EN_d$, versus IR, $IR_d$, are shown in Fig. 3. Data is provided for both scanners, for iterations of 4, 10/12, 15, and 20, for both reconstructions options (No-RM/RM) and for the smallest cylindrical inserts of diameter 4 and 6 mm. $EN_d$ and $IR_d$ increases with the iterations and a reduction of $IR_d$ and $EN_d$ is seen with the use of RM, as in Fig. 2, although the reduction of $EN_d$ is less than $IR_d$. The gradient, the relative increase in $EN_d$ to $IR_d$ with iterations, is both scanner (TrueV $>$ HRRT), reconstruction option (RM $>$ No-RM) and insert size (4 mm $>$ 6 mm) dependent.

The COV of the CRC estimated using the 50 bootstrap realizations for: the 4, 6, 8, and 12 mm and cold 25 mm inserts, both scanners and both reconstruction options are shown in Table I. The general trend is a reduction of COV as the size of the cylinder is increased. HRRT values are modestly higher to those on the TrueV and the use of RM decreases COV slightly.

### *C. Qualitative Comparison of Patient Data*

$T_1$-weighted contrast enhanced coronal and sagittal MRI image slices for patient D with corresponding co-registered summed 30-min FDG PET images of the first and third scan on the HRRT and the second scan on the TrueV scanner, with and without RM, are shown in Fig. 4. Similar transaxial and coronal slices of patient A for FLT PET images are shown in Fig. 5. The images are shown for same level of contrast saturation and images of the scans 2 and 3 have been decay corrected to that of the first scan.

For FDG, the HRRT images offer finer delineation of anatomical features in comparison to the TrueV images, for

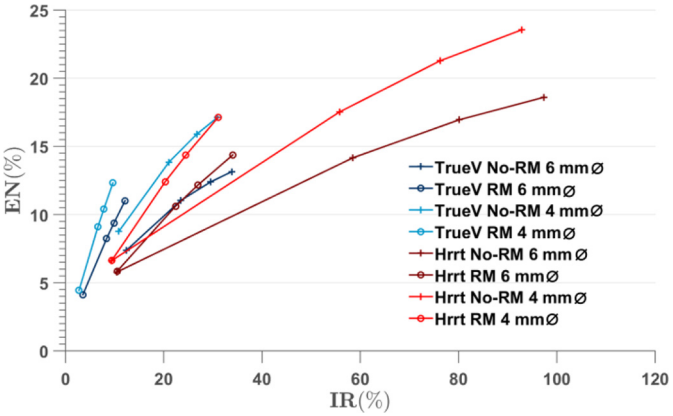


Fig. 3. Mean EN versus mean IR in background curves for cylinders 6 and 4-mm diameter on both scanners and both reconstruction methods (No-RM and RM). Analysis performed on images reconstructed for iterations 4, 10/12, 15, 20 (21 subsets for the TrueV and 16 subsets for the HRRT).

instance in the delineation of cortical folds, both without and with RM. This was the case for all the participants and for all reconstructed images and scans. For the TrueV images with RM, there is an apparent elevation of activity toward the edge of the brain and which is similar to the overshooting effect observed at the edge of the Esser phantom data (purple arrows). Any similar effect with the HRRT and RM is not as noticeable.

For FLT, uptake in the bone marrow of the skull, vertebras and sphenoid bones was high whilst uptake in the brain was very low as expected. This was seen for all scans and reconstructions methods. Visually, it would appear that uptake in sphenoid bone marrow (brown arrows) is more localized with HRRT images than with TrueV images. As with the FDG images, HRRT images without RM have an apparent higher level of noise which could potentially compromise visual assessment. For the VS lesions, which are extracranial tumors and hence outside the BBB, uptake was observed but lower than the uptake with FDG. In Fig. 5, uptake of FLT within the larger left VS lesion (green arrow) can be observed in all images whilst uptake in the smaller right lesion (red arrow) is clearer with RM reconstruction for both scanners. Apparent heterogeneous uptake of FLT is observed within the left lesion (green arrows), as observed on the transaxial HRRT images with and without RM and on the TrueV images without RM, with the uptake apparently higher in three focal areas. For the TrueV images with RM these focal areas are less distinct and start to merge together. With the RM images for both the HRRT and the TrueV there is reduction of apparent voxel noise in comparison to images without RM, but with more correlated noise where fluctuations are clustered into areas.

### D. Quantitative Comparison of Tumor Uptake

Five out of the six patients have bilateral VS lesions, with the remaining patient C only having a lesion on their right side following previous surgical removal of the left lesion. For the 50 bootstrap realizations, the mean and standard deviation of the $SUV_{mean}$ of FDG within MR contrast enhanced regions for these NF2 patients during scan 2 (approximately 75–105 min post injection) are shown in Table II, with the data interpolated from scans 1 and 3 for the scanner not used during this period.

TABLE I
COV (%) OVER 50 REALIZATIONS OF THE CRC FOR THE SET 2 ACQUISITION FOR THE HRRT AND TRUEV FOR CYLINDRICAL INSERTS OF 4, 6, 8, 12, AND 25-mm DIAMETER FOR ITERATIONS OF 10 (NO-RM) AND 12 (RM) (21 SUBSETS FOR THE TRUEV AND 16 SUBSETS FOR THE HRRT)

| | CRC COV (%) - Cylinder diameter size | | | | |
|---|---|---|---|---|---|
| Scanner /reconstruction method | 4 mm | 6 mm | 8 mm | 12 mm | 25 mm |
| HRRT No-RM | 24.4 | 6.7 | 4.4 | 2.4 | 0.7 |
| HRRT RM | 22.7 | 6.5 | 3.9 | 2.4 | 0.6 |
| TrueV No-RM | 20.3 | 6.0 | 3.1 | 1.5 | 0.4 |
| TrueV RM | 19.6 | 5.4 | 2.9 | 1.4 | 0.3 |

In most cases (9 of 11), higher FDG uptake values are seen with the TrueV data than with the HRRT (No-RM) [range $-5\%$ to $105\%$, mean $= 22\%$, $p = 0.049$ (two tailed paired $t$-test)]. When RM is used on the HRRT, notable reductions of uptake are seen in four lesions with low uptake (A-right, D-left, E-left, and F-Right), whilst the uptake remains broadly unchanged in other lesions [differences range $-42\%$ to $5\%$, mean $= -10\%$, not significant (NS)]. A similar pattern is observed on the TrueV-RM data, although with a bit more variability (range $-37\%$ to $10\%$, mean $= -8\%$, NS).

Fig. 6 shows a transaxial section through the bilateral lesions of patient D, the patient which showed the largest differences between the two scanners. Since the uptake in the brain is very high, these images have been windowed to saturate brain levels. Both lesions are close to the brain resulting in the potential for contaminating spill in with this effect likely to be larger for the left lesion due to the lower uptake levels (black arrows). Higher uptake levels extending from the vicinity of the brain into the lesion are observed with the TrueV when compared to the HRRT and consistent with its lower resolution and of the TrueV and greater spill-in. Greater heterogeneity of FDG uptake is observed within the right lesion on the HRRT images. The use of RM with the TrueV causes the uptake to apparently group into three points, but this distribution is not consistent with the heterogeneity seen with the HRRT.

Uptake values within the contrast enhanced lesions for FLT during scan 2 are shown in Table III. For the No-RM case, higher uptake values are observed on the TrueV images in comparison to HRRT images [range $-10\%$ to $+68\%$, mean $= +21\%$, $p = 0.022$ (two tailed paired $t$-test)]. RM image reconstruction increases uptake for most VS lesions on the HRRT (range $-61\%$ to $+24\%$, mean $= +4\%$, $p = 0.01$) and for the TrueV (range $-27\%$ to $+36\%$, mean $= +16\%$, $p = 0.02$), in contrast to FDG. However, a decrease is observed in those lesions where the uptake was low as in E-left and F-right with a reduction to $-38\%$ and $-61\%$ when RM is used on the HRRT, respectively.

## IV. Discussion and Conclusion

### A. Discussion

We have conducted a direct comparison between a brain dedicated PET scanner, the HRRT, which is capable of

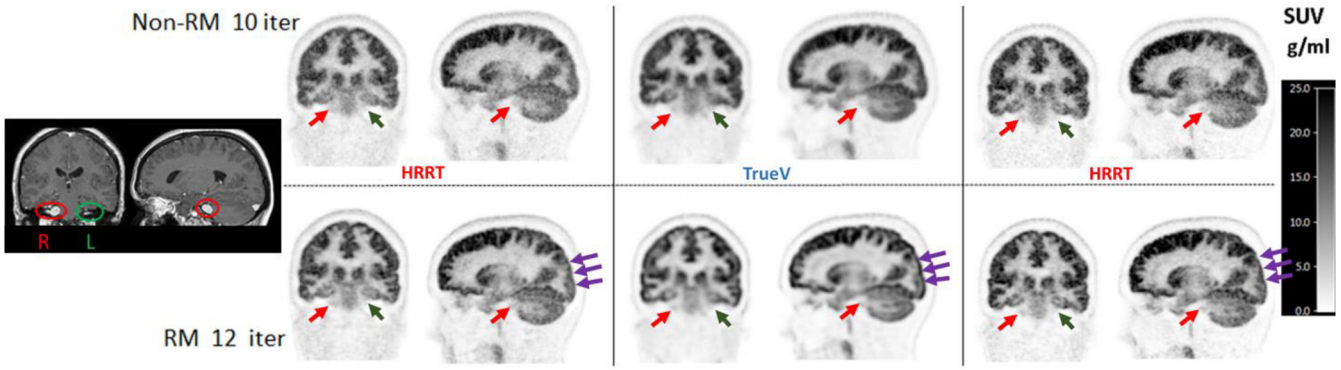


Fig. 4. Co-registered contrast enhanced MR (far left) and FDG images of an NF2 patient (patient D) scanned on both HRRT (scans 1 and 3—left and right columns) and the TrueV (scan 2—middle column). Coronal and sagittal sections are shown both without RM (top row—10 iterations) and with RM (bottom row—12 iterations). The red and green circles/arrows on the MRI/PET images highlight the location of bilateral VS lesions. The purple arrows show possible Gibb's artifacts with the TrueV and RM with similar effect not as noticeable on the HRRT and RM images. PET images are decay corrected to injection time and expressed as SUV (g/ml).

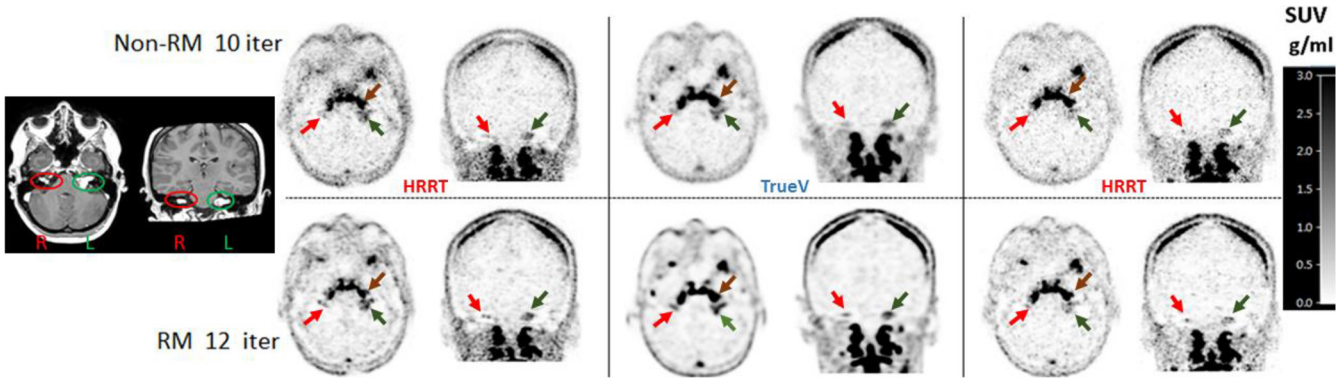


Fig. 5. Co-registered contrast enhanced MR (far left) and FLT images of an NF2 patient (patient A) scanned on both HRRT (scans 1 and 3—left and right columns) and the TrueV (scan 2—middle column). Transaxial and coronal sections are shown both without RM (top row—10 iterations) and with RM (bottom row—12 iterations). The red and green circles/arrows on the MRI/PET images highlight the location of bilateral VS lesions. The brown arrow highlights the location of uptake in bone marrow. PET images are decay corrected to injection time and expressed as SUV (g/ml).

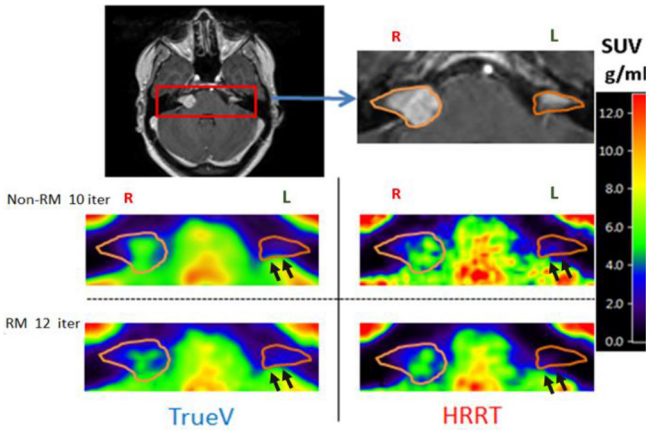


Fig. 6. Transverse sections of co-registered contrast enhanced MRI images (top) and FDG SUV uptake images through bilateral VS lesions of patient D for the TrueV (left) and the HRRT (right). Images are shown both without RM (middle row—10 iterations) and with RM (bottom row—12 iterations). For each panel the location of the ROIs used to calculate the values in Table I are shown. PET images are decay corrected to injection time and expressed as SUV (g/ml). Black arrows indicating spill in areas from the brain to VS.

achieving resolutions of 2.5-mm FWHM and a PET-CT, the Siemens Biograph Truepoint TrueV, which has a resolution around 4–5-mm FWHM. Although the TrueV is now quite an old scanner, in terms of resolution it is still representative of more modern and state-of-the-art scanners, although some recent scanners, such as the Siemens Vision, do have higher resolution. Additionally, we explored the potential benefits of RM in order to recover lost resolution. For these comparisons we used both phantom and patient data.

Previous work has compared the HRRT to other scanners with comparable resolution to that of the TrueV, such as the ECAT Exact HR+ (CTI/Siemens) [33]–[35]. However, this paper has a number of unique and important aspects: 1) the use of a modified phantom, designed to examine the benefit of high resolution scanners for the imaging of small objects; 2) the use of a complex clinical scanning protocol which controls for variability in the radiotracer injection and biological variability of the redistribution and uptake of the radiotracer; 3) the use of iterative reconstruction algorithms with RM options for both scanners; and 4) the assessment of precision using bootstrap resampling.

*1) Phantom Data:* With the Esser phantom data we observed general repeatability between the two sets of data although differences were observed for the smaller cylindrical inserts (Fig. 2). For cylindrical inserts equal or larger than 12-mm diameter when RM is not used, the TrueV and HRRT return similar CRC values (except for the 25-mm cold

TABLE II
MEAN ± STANDARD DEVIATION OVER 50 BOOTSTRAP REALIZATIONS OF SUV (g/ml) WITHIN CONTRAST ENHANCED VS LESIONS AT APPROXIMATELY 75–105 MIN FOLLOWING THE INJECTION OF FDG

| Patient | Side | HRRT | | | TrueV | | | TrueV-HRRT (No-RM) | TrueV (RM)-HRRT (No-RM) | TrueV-HRRT (RM) |
|---|---|---|---|---|---|---|---|---|---|---|
| | | No-RM | RM | Diff. mean | No-RM | RM | Diff. mean | | | |
| A | Right | 2.21±0.17 † | 1.87±0.17 † | -17% | 2.66±0.17 | 2.27±0.18 | -16% | 18% | 2% | 19% |
| | Left | 4.16±0.08 † | 4.38±0.09 † | 5% | 4.23±0.08 | 4.61±0.09 | 9% | 2% | 10% | 5% |
| B | Right | 1.81±0.11 | 1.72±0.11 | -5% | 1.73±0.08 † | 1.73±0.09 † | 0% | -5% | -5% | 0% |
| | Left | 1.99±0.06 | 1.94±0.07 | -3% | 2.21±0.05 † | 2.25±0.06 † | 2% | 10% | 12% | 15% |
| C | Right | 2.56±0.13 | 2.54±0.14 | -1% | 2.56±0.10 † | 2.36±0.10 † | -8% | 0% | -8% | -7% |
| D | Right | 3.76±0.07 † | 3.71±0.07 † | -1% | 4.47±0.07 | 4.50±0.07 | *1%* | 17% | 18% | 19% |
| | Left | 1.14±0.12 † | 0.87±0.08 † | -27% | 3.65±0.25 | 2.74±0.19 | *-29%* | 105% | 83% | 104% |
| E | Right | 2.65±0.17 † | 2.64±0.18 † | 0% | 3.12±0.12 | 3.45±0.16 | 10% | 16% | 26% | 27% |
| | Left | 1.21±0.30 † | 0.99±0.22 † | -20% | 1.78±0.33 | 1.21±0.23 | -37% | 38% | 1% | 21% |
| F | Right | 0.60±0.14 | 0.39±0.09 | -42% | 0.87±0.12 † | 0.63±0.07 † | -32% | 36% | 4% | 46% |
| | Left | 2.81±0.23 | 2.95±0.28 | 5% | 2.96±0.18 † | 3.29±0.24 † | 10% | 5% | 16% | 11% |
| Mean | | *2.26±0.33††* | *2.18±0.37††* | *-10%* | *2.75±0.33††* | *2.64±0.38††* | *-8%* | *22%* | *14%* | *24%* |

†Theses values have been linear interpolated from measurements during scan 1 and scan 3.
††Mean±SE (Standard error of the mean).
% Differences calculated as: (mean A- Mean B)/0.5(mean A+ Mean B).

TABLE III
MEAN ± STANDARD DEVIATION OVER 50 BOOTSTRAP REALIZATIONS OF SUV (g/ml) WITHIN CONTRAST ENHANCED VS LESIONS AT APPROXIMATELY 75–105 MIN FOLLOWING THE INJECTION OF FLT

| Patient | Side | HRRT | | | TrueV | | | TrueV-HRRT (No-RM) | TrueV (RM)-HRRT (No-RM) | TrueV-HRRT (RM) |
|---|---|---|---|---|---|---|---|---|---|---|
| | | No-RM | RM | Diff. mean | No-RM | RM | Diff. mean | | | |
| A | Right | 0.85±0.07 † | 1.08±0.10 † | 28% | 0.76±0.06 | 1.04±0.08 | 36% | -10% | 20% | -4% |
| | Left | 1.34±0.04 † | 1.55±0.04 † | 16% | 1.28±0.03 | 1.54±0.04 | 20% | -4% | 14% | -1% |
| B | Right | 0.69±0.07 | 0.81±0.08 | 17% | 0.72±0.05 † | 0.91±0.06 † | 26% | 4% | 28% | 12% |
| | Left | 0.92±0.03 | 1.05±0.03 | 14% | 0.96±0.03 † | 1.16±0.03 † | 21% | 4% | 23% | 10% |
| C | Right | 1.15±0.06 | 1.33±0.07 | 16% | 1.43±0.06 † | 1.64±0.08 † | 15% | 22% | 35% | 21% |
| D | Right | 1.65±0.04 † | 1.82±0.03 † | *10%* | 1.70±0.04 | 2.01±0.04 | *18%* | 2% | 19% | 9% |
| | Left | 0.81±0.08 † | 0.96±0.09 † | *18%* | 1.10±0.08 | 1.34±0.12 | *22%* | 30% | 49% | 33% |
| E | Right | 1.21±0.08 | 1.42±0.10 | 17% | 1.87±0.06 † | 2.42±0.08 † | 29% | 43% | 66% | 52% |
| | Left | 0.53±0.17 | 0.36±0.14 | -32% | 0.75±0.14 † | 0.73±0.13 † | -2% | 34% | 32% | 68% |
| F | Right | 0.16±0.06 † | 0.09±0.04 † | -47% | 0.33±0.05 | 0.24±0.04 | -27% | 68% | 39% | 94% |
| | Left | 1.00±0.12 † | 1.19±0.14 † | 20% | 1.47±0.09 | 1.67±0.13 | 14% | 38% | 51% | 33% |
| Mean | | *0.94±0.12††* | *1.06±0.15††* | *4%* | *1.12±0.14††* | *1.34±0.18††* | *16%* | *21%* | *34%* | *30%* |

†Theses values have been linear interpolated from measurements during scan 1 and scan 3.
††Mean±SE (Standard error of the mean).
% Differences calculated as: (mean A- Mean B)/0.5(mean A+ Mean B).

cylinder with better recovery for the TrueV). The cylindrical inserts used in this phantom were 40-mm long, which meant that the axial resolution was not tested and compared. When RM is used for these larger cylinders, the TrueV gives better recovery than HRRT RM. This is probably as a result of the more aggressive resolution model used with the TrueV. For smaller regions the recovery with the HRRT is notably better, especially when using RM. This was also seen visually with the HRRT images showing better delineation of the 4-mm cylinder (Fig. 1). RM reconstruction was unable to recover this loss for the TrueV with Gibbs artifacts observed (Fig. 1 purple arrows). This is not surprising since the intrinsic lower resolution of the TrueV scanner means that it is unable to measure the high spatial frequencies used to characterize higher resolution images. The limited number of iterations conducted together with the slow convergence of the high spatial frequencies means that the high frequencies are not fully restored and Gibbs artifacts are observed [18].

When assessing the precision of CRC we observed that COV was more dependent on the cylinder size than the reconstruction methods or scanner (Table I). IR is commonly used in the literature to describe image noise and for large regions over homogenous structures it is a good measure of voxel noise but in addition to this metric we have provided estimates of

EN calculated from bootstrap listmode resampling of the set 2 phantom data, versus IR for the two smallest cylindrical inserts (Fig. 3). The use of RM with 4–20 iterations decreases both $EN_d$ and $IR_d$ as measured in the background of the phantom in comparison to No-RM (Fig. 3). Previously increases in $EN_d$ with RM have been proposed [11], the opposite of what we observed, although further iterations could result in such increases. This figure also shows a monotonic relationships with iterations (i.e., IR is a good relative indicator of changes in EN with iterations), but shows that the gradient of these relationships are dependent on region size, scanner and whether RM is used (i.e., care needs to be taken when comparing IR across such cases). Specifically, when comparing CRC versus noise relationships with the use of RM, different results could be obtained when noise is defined as IR or EN [32].

*2) Patient Data:* For the clinical datasets, patients were scanned using both the TrueV and the HRRT scanners in a manner that permitted us to compare differences in FDG and FLT uptake within VS lesions. The diameter of these VS lesions varied among participants and locations (6–20-mm diameter size). Even though the size of the lesions might not be regarded as too small to be challenging to be imaged with conventional PET cameras, the proximity of these lesions to the brain for FDG and to the bone marrow within the sphenoid for FLT, it was postulated that high resolution could be desirable to minimize spill-in [36].

Subjective visual assessment of the clinical images confirmed the higher resolution of the HRRT showing apparent better cortical gray matter and brain stem nuclei contrast for FDG. Within the VS lesions, higher mean activity concentrations were observed for FDG with the TrueV compared to the HRRT with differences highly variable (Table II). This is most likely due to differential spill-in of activity from the brain and the lower resolution of the TrueV, with the variability a consequence of the size, the uptake of FDG within the lesions and the proximity of the lesion to the brain. Consistent with this observation the use of RM reconstruction resulted in reduced measured uptake for both scanners. As observed with the phantom data, the use of RM on both scanners did not change significantly the precision of the lesion measurements as determined using bootstrap resampling (Tables II and III) with the precision likely influenced by uptake contrast and lesion size.

Overall the data shown in Table II suggest that there are benefits of using higher resolution scanners to reduce the effects of spill in from the brain with FDG with the greatest impact seen for lesions with low uptake (D-left, E-left, and F-right), and visually observed in Fig. 6 for left lesion (black arrows).

For FLT similar higher mean activity concentrations were observed with the TrueV compared to the HRRT. One interpretation is that this is due to spill-in from the bone marrow uptake. However, this interpretation is not consistent with the observation that the use of RM reconstruction resulted in increases in measured uptake in the VS lesions for both scanners which suggests that the reduction in spill-in is less than the increase due to reduced partial volume. Consequently there are likely to be other factors explaining the higher uptake with the TrueV. One possible conjectured explanation is that the HRRT, due to the larger number of possible LORs, the relatively smaller voxel sizes and the relatively sparse system matrix used in image reconstruction for this scanner is potentially more susceptible to count dependent bias where areas of high uptake are underestimated whilst areas of low uptake are overestimated [16], [37]. This explanation is supported by the phantom data with higher CRC values seen in the cold 25-mm cylinder for the TrueV (No-RM).

*3) Benefits of Higher Resolution Scanners:* The phantom data demonstrated that there is the potential for high resolution scanners to better image small high contrast regions. The patient data demonstrated that contaminating spill-in from surrounding tissues could also be reduced and that we observed apparent heterogeneous uptake of the radiotracers within the contrast enhancing VS lesions for which higher resolution scanners could provide benefit. Taking together there is certainly the potential for higher resolution scanners to have value.

However, the voxels of the higher resolution images from the HRRT were consistently noisier despite the high sensitivity of this scanner [1]. With equivalent reconstruction implementations, increased noise should be expected with higher resolution requiring more count data to get equivalent precision of activity concentrations within a smaller volume. Consequently the increased resolution comes at a price and whether it is of benefit is likely to be application dependent and whether noise or low contrast due to poor resolution is more limiting. Consequently further development are needed such as hardware features that improve sensitivity, that are now been implemented in the NeuroPET system by Photo Diagnostic Systems which uses slightly bigger crystal detectors, DOI discrimination, and SiPM technology to provide an increase in sensitivity with only a small tradeoff in the spatial resolution compared to that of the HRRT [5].

*4) Benefit of Resolution Modeling Image Reconstruction:* The phantom data showed that improvements in contrast recovery are possible and the clinical data suggested that RM could reduce spill-in from surrounding tissues. The use of RM image reconstruction also results in images with reduced voxel variance (IR) which can be of benefit in the identification of lesions [38]. However, such improvements are limited with the contrast recovery of the smallest cylinders with TrueV data and RM clearly inferior to that of the HRRT.

Additionally the use of RM comes with the penalty of a more correlated noise structure and the potential for hyper-intensities, so called Gibbs artifacts, at high contrast boundaries [11]. This was observed both with the phantom data and for the FDG clinical data for TrueV images with RM. The correlated noise structure also has the potential to alter the heterogeneous distribution of activity within lesions. Activity within the VS lesions for TrueV images with RM sometimes clustered into discrete areas which did not correspond to any heterogeneity seen with the higher resolution HRRT images (Fig. 6) or where discrete focal uptake tend to be joined together following RM (Fig. 5, TrueV, left lesion). This has been previously observed with hot rod phantom data [39] which can be a consequence of a more spatially

correlated noise introduced with RM. Similar observations were not seen with the HRRT images with RM, most likely due to the conservative nature of the resolution model used in this implementation.

Overall and in view of our results (visual assessment, improvements in CRC, repeatability in patient and phantom data, and noise characterization) we suggest that a conservative approach which is only able to partly recover lost resolution like the one on the HRRT should be considered. However, the conservative RM of the HRRT also has detractors [40] where RM on the HRRT has been reported to show variability (which will affect repeatability measurements) when imaging small objects (use of HRRT in scanning rats), variability which we have not observed in our work.

*5) Limitations:* This paper has a number of limitations. The clinical data is for only 6 NF2 patients, 11 lesions in total. For patient data there is no knowledge on the true distribution of radioactivity. Consequently apparent heterogeneity with the VS lesions could be a consequence of random fluctuations. The HRRT and TrueV scans were necessarily conducted at different times and matched using linear interpolation which can have result in limited precision. To assess precision we have used LM bootstrap resampling techniques, which look at variability due to count statistics in the LM data. The acquisition of multiple phantom acquisitions to assess a loss of precision between independent data sets would assess other sources of measurement error and variations, such as scanner drift or experimental set up variations.

## V. Conclusion

Comparison of phantom and patient data between a conventional clinical PET-CT scanner and a dedicated high resolution brain scanner, the HRRT, has shown that there is benefit of high resolution scanners to reduce the partial volume effect and spill-in from surrounding tissues for small structures and lesions. However, this comes with the consequence of higher voxel noise. RM image reconstruction to restore PET-CT can provide some benefit but is unable to achieve the resolution performance of the HRRT, and has the potential for introducing image artifacts.

## Acknowledgment

The authors would like to thank P. Braithwaite and R. Anup for their efforts and help in the recruitment of patients at the Highly Specialised Commissioned NF2 Service, Central Manchester University Hospital NHS Foundation Trust.

## References

[1] H. W. de Jong *et al.*, "Performance evaluation of the ECAT HRRT: An LSO-LYSO double layer high resolution, high sensitivity scanner," *Phys. Med. Biol.*, vol. 52, no. 5, pp. 1505–1526, Mar. 2007.

[2] S. Blinder *et al.*, "Influence of depth of interaction on spatial resolution and image quality for the HRRT," in *Proc. IEEE Nucl. Sci. Symp. Conf. Rec.*, vol. 3, 2005, p. 5.

[3] J. M. Anton-Rodriguez *et al.*, "Comparison of depth of interaction encoding and resolution modelling image reconstruction in high resolution PET imaging," in *Proc. IEEE Nucl. Sci. Symp. Med. Imag. Conf. Rec.*, 2013, pp. 1–6.

[4] J. J. van Sluis *et al.*, "Performance characteristics of the digital biograph vision PET/CT system," *J. Nucl. Med.*, Jan. 2019. doi: 10.2967/jnumed.118.215418.

[5] K. S. Grogg *et al.*, "NEMA and clinical evaluation of a novel brain PET-CT scanner," *J. Nucl. Med.*, vol. 57, no. 4, pp. 646–652, Dec. 2016.

[6] *OncoVision*. Accessed: Sep. 2019. [Online]. Available: http://oncovision.com/caremibrain/

[7] A. J. Gonzalez *et al.*, "Initial results of the MINDView PET insert inside the 3T mMR," *IEEE Trans. Radiat. Plasma Med. Sci.*, vol. 3, no. 3, pp. 343–351, May 2019.

[8] N. Belcari *et al.*, "Design and detector performance of the PET component of the TRIMAGE PET/MR/EEG scanner," *IEEE Trans. Radiat. Plasma Med. Sci.*, vol. 3, no. 3, pp. 292–301, May 2019.

[9] C. E. Bauer *et al.*, "Concept of an upright wearable positron emission tomography imager in humans," *Brain Behav.*, vol. 6, no. 9, 2016, Art. no. e00530.

[10] A. J. González, F. Sánchez, and J. M. Benlloch, "Organ-dedicated molecular imaging systems," *IEEE Trans. Radiat. Plasma Med. Sci.*, vol. 2, no. 5, pp. 388–403, Sep. 2018.

[11] A. Rahmim, J. Qi, and V. Sossi, "Resolution modeling in PET imaging: Theory, practice, benefits, and pitfalls," *Med. Phys.*, vol. 40, no. 6, 2013, Art. no. 064301.

[12] V. Y. Panin, F. Kehren, C. Michel, and M. Casey, "Fully 3-D PET reconstruction with system matrix derived from point source measurements," *IEEE Trans. Med. Imag.*, vol. 25, no. 7, pp. 907–921, Jul. 2006.

[13] C. Comtat *et al.*, "Image based resolution modeling for the HRRT OSEM reconstructions software," in *Proc. IEEE Nucl. Sci. Symp. Med. Imag. Conf. Rec.*, 2008, pp. 4120–4123.

[14] F. C. Sureau *et al.*, "Impact of image-space resolution modeling for studies with the high-resolution research tomograph," *J. Nucl. Med.*, vol. 49, no. 6, pp. 1000–1008, 2008.

[15] O. V. Olesen *et al.*, "Spatial resolution of the HRRT PET scanner using 3D-OSEM PSF reconstruction," in *Proc. IEEE Nucl. Sci. Symp. Med. Imag. Conf. Rec.*, Orlando, FL, USA, 2009, pp. 3789–3790.

[16] M. D. Walker *et al.*, "Bias in iterative reconstruction of low-statistics PET data: Benefits of a resolution model," *Phys. Med. Biol.*, vol. 56, no. 4, pp. 931–949, 2010.

[17] A. Varrone *et al.*, "Advancement in PET quantification using 3D-OP-OSEM point spread function reconstruction with the HRRT," *Eur. J. Nucl. Med. Mol. Imag.*, vol. 36, no. 10, pp. 1639–1650, 2009.

[18] A. Rahmim and J. Tang, "Noise propagation in resolution modeled PET imaging and its impact on detectability," *Phys. Med. Biol.*, vol. 58, no. 19, p. 6945, 2013.

[19] K. Thielemans *et al.*, "Impact of PSF modelling on the convergence rate and edge behaviour of EM images in PET," in *Proc. IEEE Nucl. Sci. Symp. Med. Imag. Conf. Rec.*, 2010, pp. 3267–3272.

[20] B. W. Jakoby *et al.*, "Physical performance and clinical workflow of a new LSO HI-REZ PET/CT scanner," in *Proc. IEEE Nucl. Sci. Symp. Med. Imag. Conf. Rec.*, vol. 5, 2007, pp. 3130–3134.

[21] C. Knoess *et al.*, "Evaluation of single photon transmission for the HRRT," in *Proc. IEEE Nucl. Sci. Symp. Conf. Rec.*, vol. 3, 2003, pp. 1936–1940.

[22] D. G. R. Evans, "Neurofibromatosis type 2 (NF2): A clinical and molecular review," *Orphanet J. Rare Diseases*, vol. 4, no. 1, p. 16, 2009.

[23] J. M. Anton-Rodriguez *et al.*, "[18F]fluorothymidine and [18F]fluorodeoxyglucose PET imaging demonstrates uptake and differentiates growth in neurofibromatosis 2 related vestibular schwannoma," *Otol. Neurotol.*, Apr. 2019. [Online]. Available: https://journals.lww.com/otology-neurotology/Abstract/publishahead/_18F_fluorothymidine_and__18F_fluorodeoxyglucose.96496.aspx. doi: 10.1097/MAO.0000000000002272.

[24] P. J. Markiewicz, A. J. Reader, and J. C. Matthews, "Assessment of bootstrap resampling performance for PET data," *Phys. Med. Biol.*, vol. 60, no. 1, pp. 279–299, 2015.

[25] C. Lartizien, J.-B. Aubin, and I. Buvat, "Comparison of bootstrap resampling methods for 3-D PET imaging," *IEEE Trans. Med. Imag.*, vol. 29, no. 7, pp. 1442–1454, Jul. 2010.

[26] K. Herholz, R. Evans, J. Anton-Rodriguez, R. Hinz, and J. C. Matthews, "The effect of 18F-florbetapir dose reduction on region-based classification of cortical amyloid deposition," *Eur. J. Nucl. Med. Mol. Imag.*, vol. 41, no. 11, pp. 2144–2149, Nov. 2014.

[27] H. M. Hudson and R. S. Larkin, "Accelerated image reconstruction using ordered subsets of projection data," *IEEE Trans. Med. Imag.*, vol. 13, no. 4, pp. 601–609, Dec. 1994.

[28] I. K. Hong *et al.*, "Ultra fast symmetry and SIMD-based projection-backprojection (SSP) algorithm for 3-D PET image reconstruction," *IEEE Trans. Med. Imag.*, vol. 26, no. 6, pp. 789–803, Jun. 2007.

[29] S. H. Keller, C. Svarer, and M. Sibomana, "Attenuation correction for the HRRT PET-scanner using transmission scatter correction and total variation regularization," *IEEE Trans. Med. Imag.*, vol. 32, no. 9, pp. 1611–1621, Sep. 2013.

[30] J. M. Anton-Rodriguez *et al.*, "Investigation of motion induced errors in scatter correction for the HRRT brain scanner," in *Proc. IEEE Nucl. Sci. Symp. Med. Imag. Conf. Rec.*, 2010, pp. 2935–2940.

[31] *NU 2-2018 Performance Measurements of Positron Emission Tomographs (PET)*, Nat. Elect. Manuf. Assoc., Arlington, VA, USA, 2018.

[32] S. Tong, A. M. Alessio, and P. E. Kinahan, "Noise and signal properties in PSF-based fully 3D PET image reconstruction: An experimental evaluation," *Phys. Med. Biol.*, vol. 55, no. 5, pp. 1453–1473, 2010.

[33] F. H. P. van Velden *et al.*, "Comparison of HRRT and HR+ scanners for quantitative (R)-[11C]verapamil, [11C]raclopride and [11C]flumazenil brain studies," *Mol. Imag. Biol.*, vol. 17, no. 1, pp. 129–139, Feb. 2015.

[34] M. Schain *et al.*, "Quantification of serotonin transporter availability with [11C]MADAM—A comparison between the ECAT HRRT and HR systems," *Neuroimage*, vol. 60, no. 1, pp. 800–807, Mar. 2012.

[35] F. H. P. van Velden *et al.*, "HRRT versus HR+ human brain PET studies: An interscanner test-retest study," *J. Nucl. Med.*, vol. 50, no. 5, pp. 693–702, May 2009.

[36] M. Soret, S. L. Bacharach, and I. Buvat, "Partial-volume effect in PET tumor imaging," *J. Nucl. Med.*, vol. 48, no. 6, pp. 932–945, 2007.

[37] I. Hong, S. Cho, C. J. Michel, M. E. Casey, and J. D. Schaefferkoetter, "Complementary frame reconstruction: A low-biased dynamic PET technique for low count density data in projection space," *Phys. Med. Biol.*, vol. 59, no. 18, pp. 5441–5455, Sep. 2014.

[38] D. J. Kadrmas *et al.*, "Experimental comparison of lesion detectability for four fully-3D PET reconstruction schemes," *IEEE Trans. Med. Imag.*, vol. 28, no. 4, pp. 523–534, Apr. 2009.

[39] F. A. Kotasidis *et al.*, "Single scan parameterization of space-variant point spread functions in image space via a printed array: The impact for two PET/CT scanners," *Phys. Med. Biol.*, vol. 56, no. 10, pp. 2917–2942, 2011.

[40] S. A. Blinder, K. Dinelle, and V. Sossi, "Scanning rats on the high resolution research tomograph (HRRT): A comparison study with a dedicated micro-PET," *Med. Phys*, vol. 39, no. 8, pp. 5073–5083, Aug. 2012.